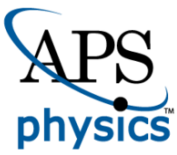

Electronic Structure Changes across the Metamagnetic Transition in FeRh via Hard X-Ray Photoemission

A. X. Gray, D. W. Cooke, P. Krüger, C. Bordel, A. M. Kaiser, S. Moyerman, E. E. Fullerton, S. Ueda, Y. Yamashita, A. Gloskovskii, C. M. Schneider, W. Drube, K. Kobayashi, F. Hellman, and C. S. Fadley

Phys. Rev. Lett. **108**, 257208 — Published 21 June 2012

DOI: 10.1103/PhysRevLett.108.257208

Electronic structure changes across the metamagnetic transition in FeRh via hard x-ray photoemission

A. X. Gray,[1,2,3] D. W. Cooke,[4] P. Krüger,[5] C. Bordel,[4,6] A. M. Kaiser,[2,3,7] S. Moyerman,[8] E.E. Fullerton,[8] S. Ueda,[9] Y. Yamashita,[9] A. Gloskovskii,[10] C. M. Schneider,[7] W. Drube,[10] K. Kobayashi,[9] F. Hellman,[3,4] and C. S. Fadley[2,3]

[1]*Stanford Institute for Materials and Energy Science, SLAC National Accelerator Laboratory, 2575 Sand Hill Road, Menlo Park, California 94029, USA*

[2]*Department of Physics, University of California, Davis, California 95616, USA*

[3]*Materials Sciences Division, Lawrence Berkeley National Laboratory, Berkeley, California 94720, USA*

[4]*Department of Physics, University of California, Berkeley, Berkeley, California 94720, USA*

[5]*ICB, UMR 5209, CNRS–Université de Bourgogne, BP 47870, 21078 Dijon Cedex, France*

[6]*GPM, UMR CNRS 6634, Université de Rouen, Av. de l'Université - BP12, 76801 St Etienne du Rouvray, France*

[7]*Peter-Grünberg-Institut PGI-6, Forschungszentrum Jülich GmbH, 52425 Jülich, Germany*

[8]*Center for Magnetic Recording Research, University of California, San Diego, La Jolla, California 92093*

[9]*NIMS Beamline Station at SPring-8, National Institute for Materials Science, Sayo, Hyogo 679-5148, Japan*

[10]*DESY Photon Science, Deutsches Elektronen-Synchrotron, 22603 Hamburg, Germany*

ABSTRACT

Stoichiometric FeRh undergoes a temperature-induced antiferromagnetic (AFM) to ferromagnetic (FM) transition at ~350 K. In this Letter, changes in the electronic structure accompanying this transition are investigated in epitaxial FeRh thin films via bulk-sensitive valence-band and core-level hard x-ray photoelectron spectroscopy with a photon energy of 5.95 keV. Clear differences between the AFM and FM states are observed across the entire valence-band spectrum and these are well reproduced using density functional theory. Changes in the 2*p* core-levels of Fe are also observed and interpreted using Anderson impurity model calculations. These results indicate that significant electronic structure changes over the entire valence-band region are involved in this AFM-FM transition.

The FeRh stoichiometric alloy has recently emerged as a subject of intense theoretical [1-4] and experimental [5-8] study because of its possible application in thermally-assisted magnetic recording (TAMR) [9-11]. The key property of FeRh which is instrumental for TAMR is a temperature-induced metamagnetic transition from antiferromagnetic order (AFM) to ferromagnetic order (FM) that occurs slightly above room temperature (~350 K) [12].

Although the existence of this transition in FeRh was first reported in 1938 [12], the origin of this phenomenon is still under debate. Early low-temperature specific heat measurements [13] reveal a substantial difference of the Sommerfeld coefficient γ between FM and AFM samples, which suggests an increase in the electronic density of states (DOS), $\rho(E)$, near the Fermi level (E_F), a conclusion later supported by a first-principles theoretical study [14]. This difference in γ leads to a difference in electronic entropy which has been suggested to drive the transition [14]. However, a recent surface-sensitive soft x-ray photoemission study reveals very little modification of the electronic structure in the valence-band region or in selected core-level spectra on passing through the transition (see e.g. Fig. 3 of ref. 8). These photoemission results thus could imply that mechanisms other than electronic entropy changes [13] near E_F may be responsible for driving this transition. In fact, alternate mechanisms such as spin-wave excitations [3] and an inherent instability of the Rh magnetic moment [2,4] have recently been proposed in theoretical studies, with some indications from heat capacity of this being observed experimentally [15]. It is also possible that the transition is driven and/or accompanied by more than one such phenomenon, and/or may involve significant changes over the entire valence-band region that have not yet been observed.

In connection with the soft x-ray photoemission study quoted above [8, these measurements were intrinsically very surface-sensitive, limited in depth by electron inelastic mean free paths (IMFPs) [16], and probing, on average, only 4-6 Å into the solid at the photon energies between 35 and 63 eV which were used for the valence-band measurements. As an alternate approach that we use here, bulk-sensitivity can be enhanced in photoemission by performing the measurements

at higher photon energies, thus imparting larger kinetic energies to the photoemitted electrons, with resulting longer inelastic mean-free paths (IMFPs) [16-18]. In particular, we have used hard x-ray photoemission spectroscopy (HAXPES or HXPS) with a photon energy of 5.95 keV to investigate the bulk electronic properties of a very nearly stoichiometric epitaxial film of composition $Fe_{0.98}Rh_{1.02}$. The resulting IMFPs and therefore the average probing depths are ~60 Å [16], corresponding to about 20 unit cells and ensuring a more truly bulk-sensitive measurement. Based on numerous prior experimental and theoretical studies, these IMFP estimates should also be accurate to within ±10-20% [16-18].

The FeRh film was grown epitaxially by magnetron sputtering from an equiatomic FeRh target onto an *a*-SiO_x/Si substrate coated with ion-beam assist-deposited MgO (IBAD MgO) at 573 K [19]; this IBAD growth produces a biaxially-textured MgO film onto which the epitaxial FeRh sample could be grown. The sample thickness was ~2000 Å and was post-annealed for 2 hours at 873 K. The composition of the film was determined via Rutherford back-scattering (RBS) measurements (see Figure 1(c) of the Supplementary Material for this paper [20] and core-level HAXPES analysis and found to be very near stoichiometric, at $Fe_{0.98}Rh_{1.02}$, and the film was shown to be epitaxial by four-circle X-ray diffraction (XRD) [19] and Figures 1(a,b) of ref. 20. Mössbauer spectroscopy measurements further showed only the expected CsCl (B2) order. Temperature-dependent magnetization data verified the magnetic states of the film, and a transition temperature $T_{AFM\rightarrow FM}$ of 362±8 K (Figure 1(d) of ref. 20).

HAXPES measurements were carried out at two synchrotron radiation facilities: SPring-8 in Hyogo, Japan, using the undulator beamline BL15XU [21], and a VG Scienta R4000 hemispherical analyzer, with an overall energy resolution of 230 meV, and measurement at two temperatures of 300 K, corresponding to the AFM phase; and 360±5 K (the maximum allowable with the sample manipulator), and at PETRA III, Beamline P09, in Hamburg, again with the same spectrometer but with lower energy resolution at ~350 meV and cryogenic cooling to 20 K and

higher temperature heating, to 400K, so as to more certainly span the transition completely. Although the high temperature in the Spring-8 measurements was very near the transition temperature, by comparing the two sets of data in a self-consistent way (see Figure S2(a),(b) in ref. 20), we are certain that we were at least halfway through the transition in these higher resolution measurements, and we focus on them in this manuscript. Additional comparisons of the two sets verify all of the changes on passing the AFM-to-FM transition seen in the data presented here, and we can thus be certain that the data presented here directly reflect the electronic structure that is intrinsic to each of the two magnetic phases. In Fig. 1(a) we present some of these results, for the valence band region, along with Fe 2*p* core-level data collected simultaneously to be discussed later. There are clear changes in the valence band, as well as in core-level spectra in going through the AFM to FM transition.

Our valence photoemission results were compared to calculations carried out using the density-functional theory (DFT) plane-wave pseudopotential code VASP [22], with additional details in Supplementary Materials [20]. We have assumed a perfectly-ordered FeRh alloy for computational simplicity, with lattice constants derived from theory and our x-ray diffraction data, and allowing also for the tetragonal distortion occurring in the AFM phase, as well as the cubic structure in the FM phase [20]. The calculated local magnetic moments in the FM phase are 3.2 μ_B on Fe and 1.0 μ_B on Rh, and in the AFM phase 3.1 μ_B on Fe and 0.0 μ_B on Rh, in agreement with previous theoretical and experimental results [1,2,23].

We have also calculated the spin-resolved and orbital-projected DOSs for both the AFM and FM phases and these are shown in Fig. S3 of ref. 20. In the FM state, both Fe and Rh DOSs exhibit spin-splitting, leading to the local moments mentioned above. In the AFM phase, however, the spin components at the Rh site are equal because there is no net local moment. In agreement with results from earlier theoretical studies [1,13], significant changes in the DOS are observed in going through the metamagnetic transition, and these span the full valence-band energy range. In particular, major shifts in the spectral weights of the e_g and t_{2g} Fe and Rh d

states, which dominate the DOSs, occur at the Fermi level and between 1 and 5 eV. Changes in the s and p orbitals are observed as well, but they are of much smaller magnitude.

In principle, these changes should be visible in the valence-band HAXPES data of Fig. 1(a), but we first need to consider the relative excitation probabilities of different orbitals, which can first be estimated from differential photoelectric cross sections. At a photon energy of 5.95 keV, the per-electron cross sections for the valence electrons are in ratios Rh 4*d* : Rh 5*s* : Fe 3*d* : Fe 4*s* = 1.000 : 1.154 : 0.089 : 1.067 [24,25,26], and thus we expect our valence-band spectra will be dominated by the Rh 4*d* contributions, as well as any Rh 5*s* and Fe 4*s* contributions. However, the Fe 3*d* character should also be indirectly detectable through the strong Rh 4*d* – Fe 3*d* hybridization.

In order to more quantitatively simulate the measured HAXPES valence-band spectra including these cross-section effects, we have scaled the orbital-projected DOSs (see Fig. S3 in ref. 20) by the free-atom differential cross-sections based on parameters tabulated in Ref. 24 for a photon energy of 5.95 keV, including corrections for the effects of experimental geometry and non-dipole effects that begin to play a role at these higher energies [27,28]. These results are shown in Fig. 2, and they clearly demonstrate the dominant character of the Rh 4*d* states on the spectra for both the AFM and FM phases.

In Figs. 1(a) and 1(b), we now compare the experimental AFM- and FM-phase valence-band spectra with theoretical curves based on a sum of the cross-section weighted densities of states that have then been convoluted with both a Gaussian function of FWHM=0.23 eV corresponding to the total instrumental resolution and a Lorentzian function of varying FWHM of $0.20\times(E-E_F)$ to allow for hole lifetime broadening [29,30]. AFM-FM Differences between the spectra of the two phases are also shown, with all major features labeled 1-9 for the experiment and corresponding features labeled 1’-9’ for the theory; the experimental difference is multiplied by 4 to enable better comparison with theory.

The agreement for the differences is remarkable. All of the major peaks and valleys in the experimental AFM-FM difference spectra are reproduced by theory at the correct binding energies and with the correct relative intensities; only feature 2 is stronger in experiment than in theory. Among other observations in both experiment and theory are a small decrease in the DOS at E_F (feature 1) that would directly affect heat capacity measurements; additional fine structure near the Fermi level (features 1-3), an energy shift of the two Rh 4*d*-derived peaks at 1.8 eV and 2.5 eV in the AFM phase (characterized by features 4-7), and a general energy shift of the spectral weight between 4 eV and 7 eV (features 8 and 9). The approximately fourfold overestimate in theory of the effects in these differences we can readily attribute to several factors. First, all of the changes observed experimentally between the AFM and FM phases might be slightly underestimated if the sample was not fully in the FM phase during the high temperature measurement shown here. Second, since this is a ground-state one-electron estimate, the inclusion of many-electron excitations would be expected to create spectral weight at higher binding energies (so-called incoherent peaks), thus reducing the effects seen in experiment. Third, recoil is known in HAXPES to shift energies and broaden features [31], and these effects are expected to be at the level of 0.03 and 0.06 eV for the masses of Rh and Fe, respectively; this effect also would tend to reduce the expected experimental differences. Finally, our estimate of the variation of lifetime broadening with binding energy may be conservative, with Fermi liquid theory in fact suggesting a quadratic, instead of linear, increase with binding energy [32]. As a closing comment, there is at least qualitative corroboration of features 1 and 2 in the experimental data from Ref. 7, Fig. 3(c) as converted into a similarly normalized difference spectrum, although as noted these measurements will be much more surface and wave-vector sensitive; none of features 3 to 9 is seen in this data however.

The high degree of agreement between experiment and theory allows us to further interpret the AFM-FM transition-induced changes we see in the experimental valence-band spectra (features 1-9 in Fig. 1(a)) by considering further the theoretical orbital- and spin-projected DOSs

(Fig. 2 and Fig. S3 of ref. 20) which have been used to model the photoemission spectra in Fig. 1(b). For example, feature 1 clearly arises due to the fact that the minority Fe-d (both t_{2g} and e_g) bands cross the Fermi level in the FM state, but not in the AFM state. This holds true for the Rh DOS as well due to its strong hybridization with Fe [4]; thus, the DOS in the AFM state is less than that in the FM state close to the Fermi level. Features 8 and 9, on the other hand, result from the spin-splitting of the Rh e_g states. It can be seen that the AFM-FM transition is accompanied by a shift of spectral weight in the Rh e_g states from a binding energy of ~5 eV in the AFM phase to ~4 eV in the FM phase, most obviously evidenced in the differences between the spin-down spectra. This spectral shift is also observed in the Fe e_g states, further indicating strong hybridization of the Fe and Rh orbitals. Feature 7 can be similarly explained by examining the t_{2g} states. The FM Rh t_{2g} states show a strong spin-splitting that is accompanied by a large reduction in the spin-up DOS at ~3 eV; because no such gap appears in the AFM phase, this yields the spectral difference observed in feature 7. This gap also appears in the FM Fe t_{2g} states.

Since the Fe states near the Fermi level could not be directly probed due to the dominant character of Rh 4*d* in the HAXPES spectra the Fe 2*p* core-level spectra of Fig. 3(a) are useful in providing a truly element-specific probe of Fe. Corresponding theoretical calculations based on the Anderson impurity model (AIM) that is often used to model final state screening and multiplet effects in core spectra, broadened by an estimated experimental plus lifetime contribution of 0.8 eV, are also shown in Fig. 3(b). These calculations were carried in a manner self-consistent with the valence electronic structure results shown in Figs. 1(b) and 2, with further details presented elsewhere [20]. From the projected densities of states of our band structure calculations, we find that the occupied Fe-d spin-orbitals are very well described as five spin-up electrons occupying both e_g and t_{2g}, states, and one spin-down electron in t_{2g}, that is, $(t_{2g}\uparrow)^3(e_g\uparrow)^2(t_{2g}\downarrow)^1$ with an overall designation $d^6\,{}^5T_2$. This atomic state thus locally describes the initial electronic state, with the impurity model mixing in other states with one and two ligand screening electrons. Charge fluctuations are accounted for approximately in the cluster model

via hybridization with ligand states (Fig. S3 and Table in [20]). The lineshapes of calculated spectra are in good agreement with the experimental data, with correspondences seen between features A-C in experiment and A'-C' in theory. The fact that the satellite C' is too sharp and too close to the main line is probably due to the neglect of ligand-field band widths. Small differences in experimental lineshape are observed between the AFM and FM phases. In particular, the AFM spectra shows a shoulder structure (feature labeled A in experiment) on the lower-binding energy side of the $2p_{3/2}$ peak at 707.5 eV, which gets washed out in the FM phase. Qualitatively the same change is seen in the calculated spectra (feature labeled A' in theory). This effect is due to the spin-dependence of the core-hole screening through Fe ligand electrons. Since the impurity up-spin states are filled, only down spin ligand electrons can hop to the impurity to screen the core hole in the final state. For Fe ligands, the charge transfer energy of this process is larger by the exchange splitting (~3 eV) for antiferromagnetically coupled neighbors (AFM phase) than for ferromagnetically coupled ones. This lowering of the charge transfer energy in the FM state shows up as an enhancement of the spectral intensity at the lower-binding-energy edge of the $2p_{1/2}$ peak. The enhancement of low energy screening channels is directly related to the strong increase of the Fe-DOS at the Fermi level in the FM phase (Fig. S3 in [20]). The $2p_{1/2}$ spectrum shows no fine structure in experiment, although theory predicts a doublet like A' and B', but there is a feature at ~729 eV in experiment that could be related to that at ~727 eV in theory, and to C' in origin. We note for comparison that a similar dependence of the lineshape on the magnetic state was found in Mn $2p$ spectra of $LaMnO_3$ [33], although the more metallic character of FeRh is expected to make the AIM model a less accurate description of such core-level spectra. Thus, in addition to direct experimental confirmation of the Rh valence-band-DOS behavior predicted by the DFT calculations (Fig. 1), we also indirectly confirm the change in the Fe-derived DOSs via core-level spectroscopy and AIM calculations which are consistent with the DFT model (Fig. 3).

In summary, through bulk-sensitive valence-band and core-level hard x-ray photoemission measurements, we have demonstrated that the electronic structure of FeRh indeed undergoes qualitative and quantitative changes during the metamagnetic transition from AFM to FM, and that these changes are very well predicted by first-principles DFT calculations. The excellent agreement between theory and experiment for both valence and core spectra indicate further that the electronic structure changes throughout the full valence-band manifold, thus providing a clearer picture through which to understand this transition.

Salary support for this research was supported by the U.S. Department of Energy, Office of Science, Office of Basic Energy Sciences, Division of Materials Sciences and Engineering under Contract No. DE-AC02-05CH11231 [Cooke, Bordel, Hellman and Fadley], and by the ARO MURI Grant W911-NF-09-1-0398 [Kaiser]. HAXPES experiments were approved by SPring-8 NIMS Beamline Station (Proposal No. 2010A4902). The authors are grateful to HiSOR Hiroshima University and JAEA/SPring-8 for the development of HAXPES at BL15XU of SPring-8. This work was partially supported by the Nanotechnology Network Project, MEXT, Japan.

REFERENCES

1. V. L. Moruzzi and P. M. Marcus, Phys. Rev. B, **46**, 2864 (1992).
2. M. E.Gruner, E. Hoffmann, and P. Entel, Phys. Rev. B **67**, 064415 (2003).
3. R. Y. Gu and V. P. Antropov, Phys. Rev. B **72**, 012403 (2005).
4. L. M. Sandratskii and P. Mavropoulos, Phys. Rev. B **83**, 174408 (2011).
5. J.-U. Thiele, S. Maat, and E. E. Fullerton, Appl. Phys. Lett. **82**, 2859 (2003).
6. S. Maat, J.-U. Thiele, and E. E. Fullerton, Phys. Rev. B **72**, 214432 (2005).
7. C. Stamm *et al.*, Phys. Rev. B **77**, 184401 (2008).
8. J.-S. Lee *et al.*, Phys. Rev. B **82**, 224410 (2010).
9. S. Cumpson, P. Hidding, and R. Coehoorn, IEEE Trans. Magn. **36**, 2271 (2000).
10. J. J. M. Ruigrok *et al.*, J. Appl. Phys. **87**, 5298 (2000).
11. J.-U. Thiele *et al.*, IEEE T. Magn. **40**, 2537 (2004).
12. M. Fallot, Ann. Phys. **10**, 291 (1938).
13. P. Tu *et al.*, J. Appl. Phys. **40**, 1368 (1969).
14. C. Koenig, J. Phys. F Met. Phys. **12**, 1123 (1982).
15. David W. Cooke, C. Bordel, S. Moyerman, E.E. Fullerton, and F. Hellman, *in preparation* (2011).
16. S. Tanuma, C. J. Powell, and D. R. Penn , Surf. Interface. Anal. **43**, 689 (2011).
17. K. Kobayashi, Nucl. Instrum. Meth. A **547**, 98 (2005).
18. Z. Boekelheide *et al.*, Phys. Rev. Lett. **105**, 236404 (2010).
19. David W. Cooke *et al.*, Rev. of Sci. Instr. **82**, 023908 (2011).
20. See supplementary material at [link inserted by PRL] for details on theoretical calculations.
21. S. Ueda *et al.*, AIP Conf. Proc. **1234**, 403 (2010).

22. G. Kresse and J. Hafner, Phys. Rev. B **47**, 558 (1993); G. Kresse and J. Hafner, Phys. Rev. B **49**, 14251 (1994); G. Kresse and J. Hafner, Comput. Mater. Sci. **6**, 15 (1996); G. Kresse and J. Furthmüller, Phys. Rev. B **54**, 11169 (1996).
23. G. Shirane, R. Nathans, and C.W. Chen, Phys. Rev. **134**, A1547 (1964).
24. J. H. Scofield, Tech. Rep., LLNL Report No. UCRL-51326, (1973).
25. J.-J. Yeh and I. Lindau, At. Data Nucl. Data Tables 32, (1985).
26. G. Rossi *et al.*, Phys. Rev. B **28**, 3031 (1983).
27. M. B. Trzhaskovskaya, V. I. Nefedov, and V. G. Yarzhemsky, At. Data Nucl. Data Tables **77**, 97 (2001).
28. M. B. Trzhaskovskaya *et al.*, At. Data Nucl. Data Tables **92**, 245 (2006).
29. J. Park *et al.*, Phys. Rev. B **69**, 165120 (2004).
30. A. Toropova *et al.*, Phys. Rev. B **71**, 172403 (2005).
31. Y. Takata *et al.*, Phys. Rev. Lett. **101**, 137601 (2008).
32. R. Matzdorf, Chemical Physics **251**, 151 (2000).
33. K. Horiba *et al.*, Phys. Rev. Lett. **93**, 236401 (2004).

FIGURE CAPTIONS

Fig. 1: (a) Experimental valence-band HAXPES spectra collected with a photon energy of 5.95 keV for both AFM and FM phases at sample temperatures of 300 K and 360 K, respectively. (b) Cross-section weighted total densities of states for both AFM and FM phases, calculated in the framework of density-functional theory and broadened by convolution with Gaussian and Lorentzian functions in order to account for both experimental and hole lifetime broadening. AFM-FM differences are also shown for both theory and experiment, with the experimental curve being multiplied by 4 so as to exhibit roughly the same visual excursions.

Fig. 2: Cross-section weighted orbital-projected densities of states of FeRh in the (a) FM and (b) AFM phases, and their totals. These projected results indicate that the photoemission signal at our photon energy of 5.95 keV will be dominated by the Rh 4*d* states.

Fig. 3. (a) Experimental Fe 2*p* core-level HAXPES spectra collected with a photon energy of 5.95 keV for both AFM and FM phases at sample temperatures of 300 K and 360 K, respectively, and obtained at the same time as the spectra in Fig. 1(a). (b) Fe 2*p* spectra calculated for the AFM and FM phases using the Anderson impurity model, and broadened to allow for estimated experimental and lifetime broadening.

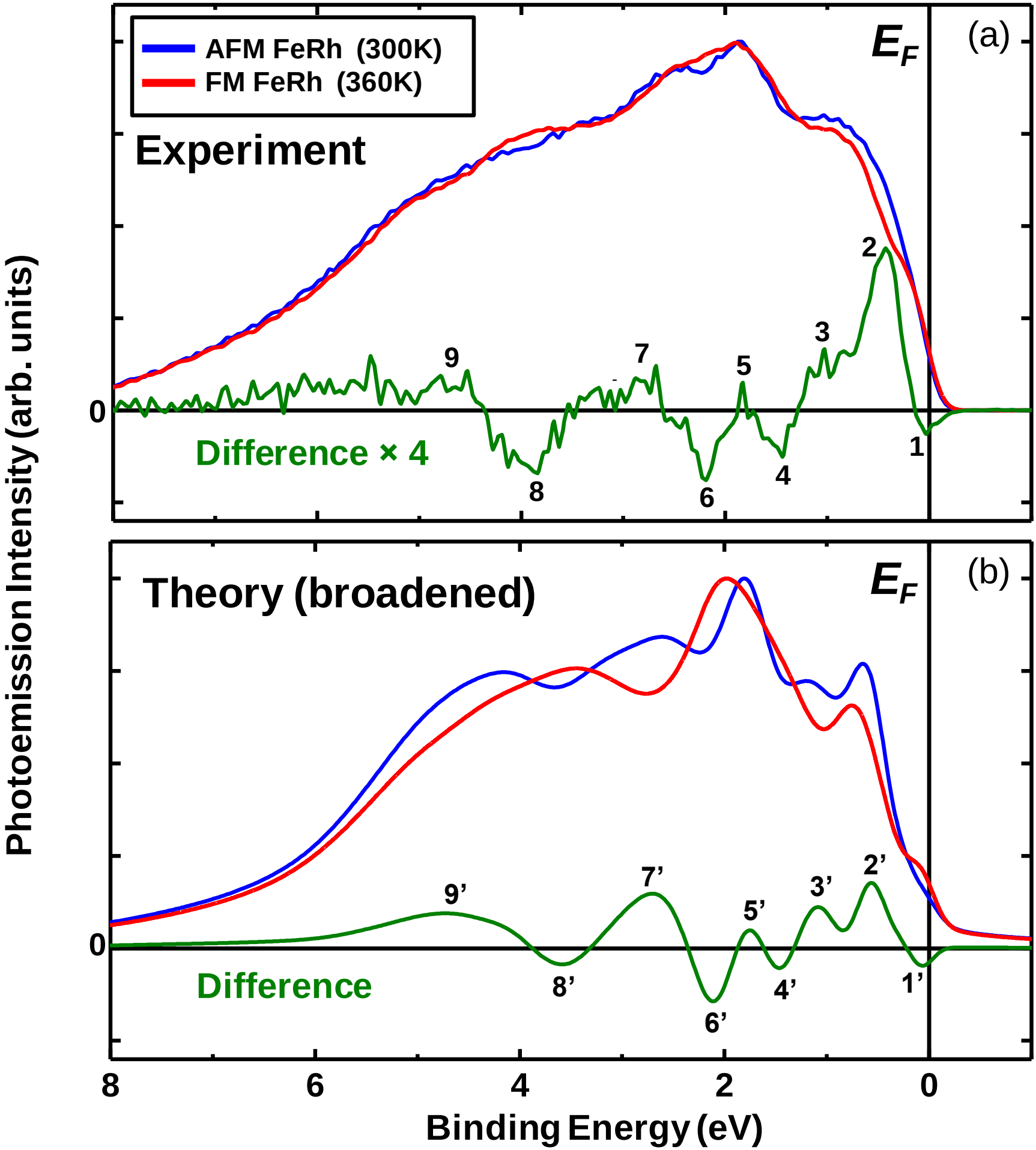
AFM FeRh (300K)
FM FeRh (360K)
Experiment
E_F
(a)
Difference × 4
1
2
3
4
5
6
7
8
9
Theory (broadened)
E_F
(b)
Difference
1'
2'
3'
4'
5'
6'
7'
8'
9'
0
0
Photoemission Intensity (arb. units)
8
6
4
2
0
Binding Energy (eV)

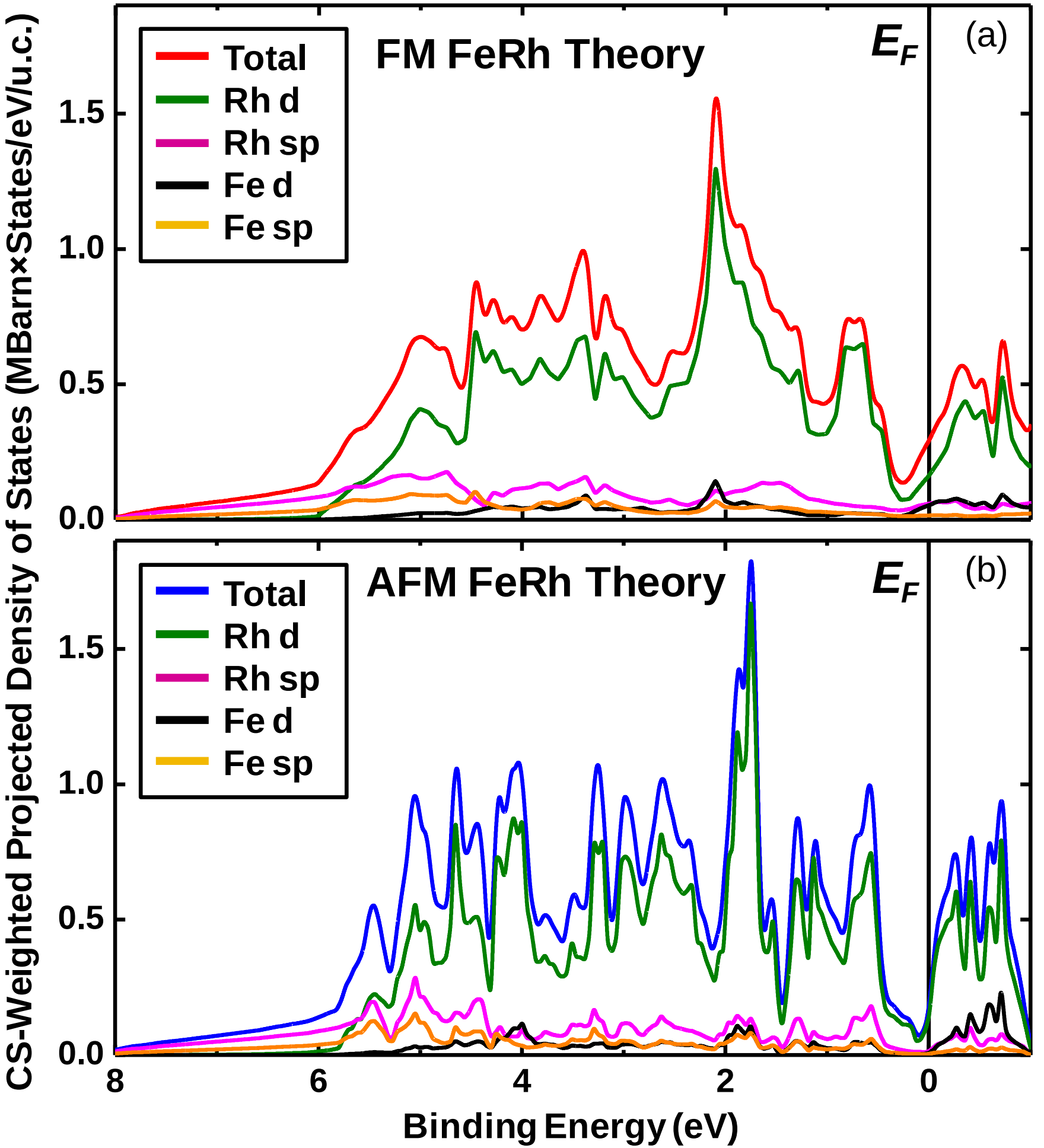
FM FeRh Theory
E_F
(a)
Total
Rh d
Rh sp
Fe d
Fe sp
AFM FeRh Theory
E_F
(b)
Total
Rh d
Rh sp
Fe d
Fe sp
CS-Weighted Projected Density of States (MBarn×States/eV/u.c.)
0.0
0.5
1.0
1.5
8
6
4
2
0
Binding Energy (eV)

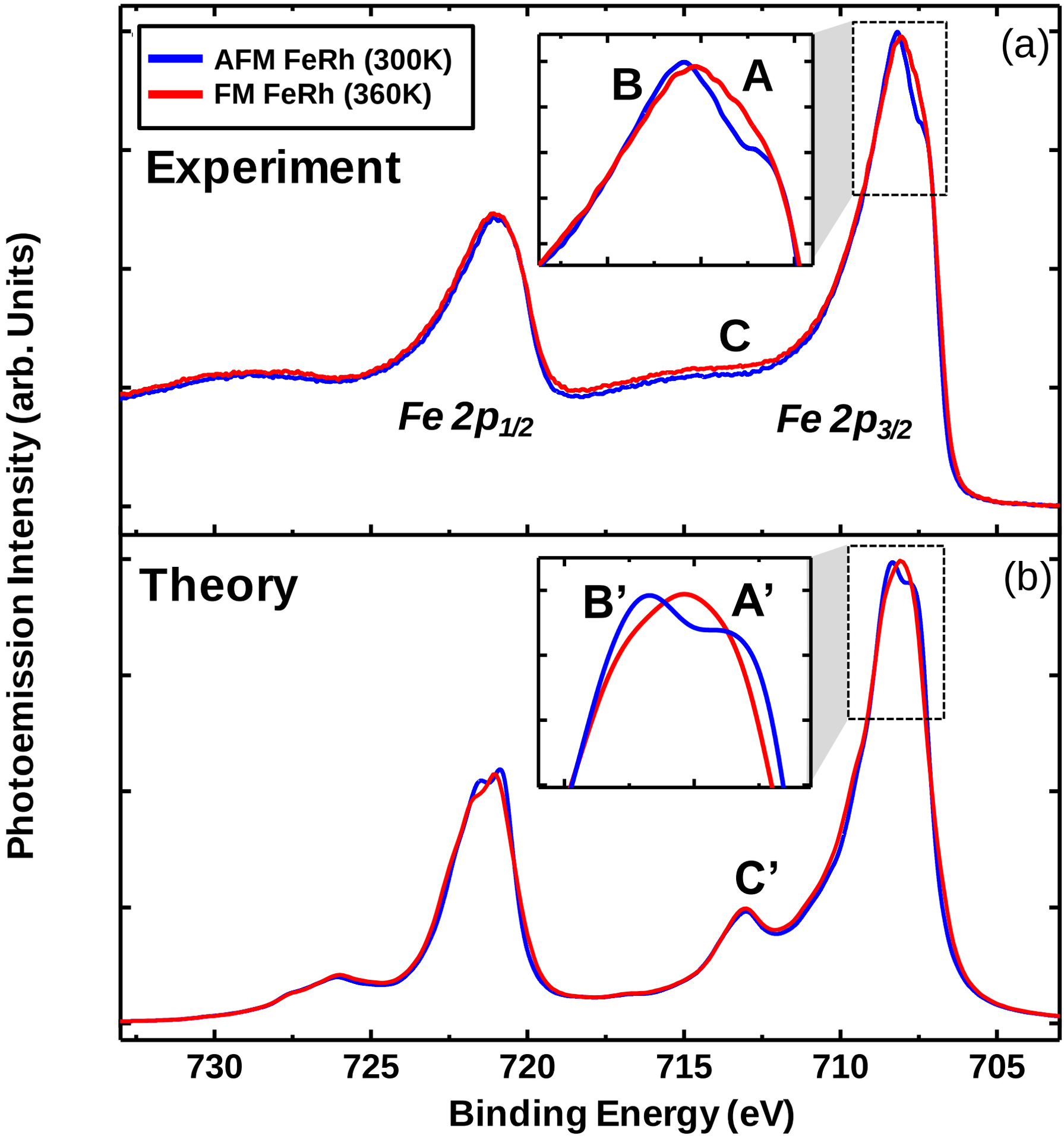
AFM FeRh (300K)
FM FeRh (360K)
Experiment
(a)
B
A
C
Fe 2p1/2
Fe 2p3/2
Theory
(b)
B'
A'
C'
Photoemission Intensity (arb. Units)
730
725
720
715
710
705
Binding Energy (eV)